

© 2016 by Bryan P. Dannowitz. All rights reserved.

NUCLEAR DEPENDENCE OF PROTON-INDUCED DRELL-YAN DIMUON  
PRODUCTION AT 120GEV AT SEAQUEST

BY

BRYAN P. DANNOWITZ

DISSERTATION

Submitted in partial fulfillment of the requirements  
for the degree of Doctor of Philosophy in Nuclear Physics  
in the Graduate College of the  
University of Illinois at Urbana-Champaign, 2016

Urbana, Illinois

Doctoral Committee:

Professor Jen-Chieh Peng, Chair  
Professor Naomi C. R. Makins, Director of Research  
Professor Michael Stone  
Professor David Ceperley

# Abstract

A measurement of the atomic mass dependence of Drell-Yan dimuons produced by 120GeV protons is presented here. Over 88,000 dimuon pairs with dimuon mass  $M \geq 4.2 \text{ GeV}$  were recorded at SeaQuest from targets  $^1H$ ,  $^2H$ ,  $C$ ,  $Fe$ , and  $W$ . The ratio of dimuon yield per nucleon for heavy nuclei versus  $^2H$ ,  $R = Y_A/Y_{^2H}$ , is sensitive to modifications in the anti-quark sea in nuclei for the case of proton-induced Drell-Yan. No nuclear modifications are observed over the target quark momentum fraction range  $0.1 \leq x_t \leq 0.45$ . These results are compared to predictions of models of the EMC effect.

*To my dog, Charlemagne.*

# Acknowledgments

This paper does not acknowledge Star Wars Episodes I-III, nor does it acknowledge Pluto as a full-on planet.

# Table of Contents

<b>List of Tables</b> . . . . .	<b>vii</b>
<b>List of Figures</b> . . . . .	<b>viii</b>
<b>List of Abbreviations</b> . . . . .	<b>ix</b>
<b>List of Symbols</b> . . . . .	<b>xi</b>
<b>Chapter 1 Introduction</b> . . . . .	<b>1</b>
<b>Chapter 2 Nucleon Internal Structure Phenomenology</b> . . . . .	<b>2</b>
2.1 Introduction . . . . .	2
2.2 <i>ep</i> Scattering . . . . .	3
2.3 The Drell-Yan Process . . . . .	3
2.3.1 The Drell-Yan Cross-Section . . . . .	6
2.3.2 Drell-Yan Kinematics . . . . .	6
2.4 The EMC Effect . . . . .	6
<b>Chapter 3 Apparatus</b> . . . . .	<b>7</b>
3.1 Apparatus Overview . . . . .	7
3.2 Main Injector Proton Beam . . . . .	8
3.3 Beam Intensity Monitor . . . . .	10
3.4 The SeaQuest Targets . . . . .	13
3.5 Focusing and Analyzing Magnets . . . . .	15
3.6 Beam Dump, Shields, and Absorbers . . . . .	16
3.7 Tracking Detectors . . . . .	17
3.8 Triggering Hodoscopes . . . . .	18
3.8.1 Overall structure . . . . .	19
3.8.2 Performance requirement . . . . .	19
3.8.3 Constructions . . . . .	20
3.8.4 Electronics . . . . .	21
3.8.5 Measurement of Performance . . . . .	21
3.8.6 Mass Resolution . . . . .	23
3.9 Triggering Matrices . . . . .	23
3.9.1 Requirements . . . . .	23
3.10 Data Acquisition Systems . . . . .	24
3.11 Data Productions . . . . .	24
3.11.1 Production Processing . . . . .	24
3.11.2 Decoding Raw Data . . . . .	24
3.11.3 Online and Offline Processing . . . . .	26
3.12 RDBMS Data Structure . . . . .	27
3.13 Data Quality . . . . .	27

<b>Chapter 4</b>	<b>PMT Upgrade</b>	<b>28</b>
4.1	Introduction: PMT Sagging	28
4.2	PMT Base Terminology and Common Characteristics	28
4.3	PMT Base Design Iterations	29
4.3.1	Original Base	29
4.3.2	Prototype Base v1	29
4.3.3	Prototype Base v2	32
4.3.4	Prototype Base v3	33
4.3.5	Prototype Base v4	34
4.4	PMT Base Comparisons	35
4.4.1	Testing Apparatus and Measurements	35
<b>Chapter 5</b>	<b>Analysis</b>	<b>36</b>
5.1	Particle Identification	36
5.2	Data Selection	36
5.2.1	Spill Level Cuts	36
5.2.2	Dimuon Level Cuts	37
5.2.3	Track Level Cuts	37
5.2.4	Other Cuts	37
5.3	Dimuon Yields	37
5.3.1	Binning of Data	37
5.3.2	Raw Yields	37
5.4	Rate Dependence and Combinatorial Background Correction	38
5.5	Empty/None Target Background Subtraction	38
5.6	Dimuon Yield Ratios	38
5.7	$ld_2$ Contamination Correction	38
5.8	Isoscalar Corrections for $^{183}W$ and $^{56}Fe$	38
<b>Chapter 6</b>	<b>Results</b>	<b>39</b>
<b>Chapter 7</b>	<b>Discussion</b>	<b>40</b>
<b>Chapter 8</b>	<b>Conclusions</b>	<b>41</b>
<b>Appendix A</b>	<b>PMT Upgrades</b>	<b>42</b>
A.1	ARGUS PMT Performance 'Sag'	42
A.2	Prototype Testing	42
A.3	Manufacturing and Installation	42
<b>Appendix B</b>	<b>MySQL Production Structure</b>	<b>43</b>
B.1	MySQL Servers	43
B.2	Atomic Schema Design	43
B.3	Merged Schemas	43
<b>References</b>		<b>44</b>

# List of Tables

2.1	Kinematic variables relevant to the Drell-Yan process . . . . .	4
3.1	Characteristics of the seven SeaQuest target positions. The “Spills/Cycle” is only a typical configuration and can vary according to needs and running configurations. The non-zero interaction length of the empty flask is due to the $51\mu\text{m}$ -thick stainless steel end-caps of the flask and the $140\mu\text{m}$ -thick titanium windows of the vacuum vessel that contains it. . . . .	14
3.2	Parameters of all hodoscope planes. $z$ -positions of half-planes are offset slightly due to slight misalignment and/or overlap of half-planes. . . . .	18
3.3	Parameters of all chambers. Those of primed planes are almost the same as of unprimed planes. The $z$ -positions of U and V planes are relative to those of X planes. . . . .	19
3.4	Combination of chambers per data taking period. . . . .	20
3.5	Performance of all DCs. That of DC1.2 is of anticipated values based on simulations, and those of the others are of measured values in Run 3. . . . .	22
3.6	Performance of all DCs. That of DC1.2 is of anticipated values based on simulations, and those of the others are of measured values in Run 3. . . . .	24
5.1	$x_2$ bin ranges . . . . .	37
5.2	Raw dimuon yields for Roadset 57 . . . . .	37



# List of Figures

2.1	(A) Deep inelastic scattering (DIS) is a $t$ -channel interaction which uses the emission of a virtual photon to probe the target hadron. (B) The similar Drell-Yan (DY) process, using the $s$ channel version of the DIS interaction, via annihilation of a beam quark with an anti-quark from the target hadron. . . . .	3
2.2	The Drell-Yan process has a large range of higher-order QCD corrections that need to be accounted for. (A) and (B) are high order $q\bar{q}$ annihilations, and (C) and (D) are gluon "Compton scattering" terms. . . . .	4
2.3	The proton's momentum distribution and the EMC Effect, with key regions highlighted. . . .	5
3.1	Spill structure of the beam delivered to SeaQuest. . . . .	9
3.2	Beam profile detailed by SWIC detectors along the NM beam line. . . . .	10
3.3	A single high-intensity event with majority of all detector elements firing off. Track reconstruction in these cases is impossible. . . . .	11
3.4	The Beam Intensity Monitor (BIM) Cerenkov counter. Measurements are in inches. . . . .	12
3.5	The layout of the target table and its seven target positions, as seen from above. . . . .	14
3.6	Perspective drawing of FMAG's aluminum coils embedded in an arrangement of iron slabs. . .	16
3.7	Spectrometer layout of FMAG, KMAG, and Detector Stations 1-4. . . . .	17
3.8	Single-plane efficiency. <i>This plot is NOT final. Should we show those of DC3m.1? Should we use a table instead of plot?</i> . . . . .	22
3.9	Single-plane position resolution. <i>This plot is NOT final. The horizontal axis has to be converted to drift distance. If the resolution of all chambers/planes is rather constant, we should use a table instead of plot.</i> . . . . .	22
4.1	(Left) Histogram of hodoscope 'hits' in a typical event; (Right) Histogram of high-intensity event, with marked sagging in the middle of the y-measuring hodoscopes . . . . .	29
4.2	The original PMT base design. . . . .	30
4.3	The (negative) voltage between subsequent stages for the original PMT base. . . . .	30
4.4	The Prototype v1 board. . . . .	31
4.5	The (negative) voltage between subsequent stages for the Prototype v1 PMT base. . . . .	32
4.6	The (negative) voltage between subsequent stages for the Prototype v2 PMT base. . . . .	32
4.7	The Prototype v3 board: 3 more transistorized stages than the Prototype v1 design. . . . .	33
4.8	The (negative) voltage between subsequent stages for the Prototype v3 PMT base. . . . .	34
4.9	The (negative) voltage between subsequent stages for the Prototype v4 PMT base. . . . .	34
4.10	Inside of a lightbox, we have our prototype board (left) wired up to a Philips XP-2008 PMT (middle), facing a fast-led source (right) . . . . .	35

# List of Abbreviations

ACNET	Accelerator control system network
BIM	Beam intensity monitor
BPM	Beam profile monitor
CEBAF	Continuous Electron Beam Accelerator Facility
CODA	CEBAF On-line Data Acquisition
DAQ	Data acquisition
DIS	Deep-inelastic scattering
DY	Drell-Yan
E906	Experiment number 906 at Fermilab National Accelerator Laboratory, a.k.a. SeaQuest
FNAL	Fermi National Accelerator Laboratory (Fermilab)
IC	Ion chamber
KTeV	Fermilab experiment that previously inhabited the NM4 experimental hall
LINAC	Fermilab Linear Accelerator
LO	Leading order
MI	(Fermilab) Main Injector
NDF	Neutral density filter
NLO	Next-to-leading order
NM	Neutrino-muon beam line
NNLO	Next-to-next-to-leading order
PDF	Parton distribution function
PMT	Photomultiplier tube
RF	Radio frequency
RFQ	Radio frequency quadrupole
SEM	Secondary emission monitor
QCD	Quantum chromodynamics

QED	Quantum electrodynamics
QIE	Charge (Q) integrator and encoder
RDBMS	Relational database management system
SQL	Structured querying language
SWIC	Segmented wire ion chamber

# List of Symbols

$\mu^+$	Positive muon
$\mu^-$	Negative muon
$J/\Psi$	The first excited state of a <i>charm-anticharm</i> meson family

# Chapter 1

## Introduction

## Chapter 2

# Nucleon Internal Structure Phenomenology

The topic of this paper, simply put, is the exploration of the momentum structure of the *nucleon*, a particle that makes up an atom's nucleus which can be either a proton ( $p$ ) or a neutron ( $n$ ). By momentum structure, I refer to the fractional momentum distributions carried by the nucleon's constituent particles, quarks and gluons.

While a complete review of the history and physics behind nucleon structure and its investigative probes is beyond the scope of this paper, a brief overview of deep-inelastic scattering and Drell-Yan will help in understanding concepts and terminology relevant to this and later chapters.

### 2.1 Introduction

The first indication that the proton may have some internal structure was in a 1933 experiment by Estermann *et al.* measuring the magnetic moment of the proton [5]. Since the proton was thought to be a point-like Dirac particle, its magnetic moment ( $\mu_p$ ) was expected to be  $\mu_p = \frac{e}{2m_p} = 1n.m.$ , or one *nuclear magneton*. The experiment resulted in a value of 2.5 n.m., leading many to reconsider the notion that the proton is indeed point-like.

Around the same time, Hideku Yukawa is credited for establishing the first theory of a *strong force*, a force binding together nucleons in a nuclei against the sizable *Coulomb* repulsion of protons []. The force was theorized to be mediated by the exchange of particles called *mesons*, and its range was limited to nuclei-scale distances, seeing as it's not observed at larger distances. Based upon the size of the nucleus, Yukawa estimated the mass of the intermediating particles to be approximately  $2 \times 10^2 m_e \approx 100 MeV$ , where  $m_e$  is the electron mass. The following year, Anderson et al. discovered the muon ( $\mu$ ) at around this mass [], which confused many, as it did not seem to partake in strong interactions. Eventually, by 1947, the meson theory was validated by the discovery of the *pion* by Powell *et al.* [], and Yukawa was awarded a Nobel Prize for his theory in 1949.

While the

The study of nucleon structure has come a long way, and at present, the proton is described as a composite particle consisting of three point-like *valence quarks* interacting with each other through exchange of gluons.

## 2.2 $ep$ Scattering

Nucleon structure is still today one of the great frontiers of nuclear physics. The primary tool used to probe the parton distribution has been Deep Inelastic Scattering (DIS), which is the scattering of a charged lepton off of a nucleus by the exchange of a virtual photon. As the energy of the exchanged photon increases, the scattering becomes inelastic and is able to resolve the partonic substructure of hadrons.

## 2.3 The Drell-Yan Process

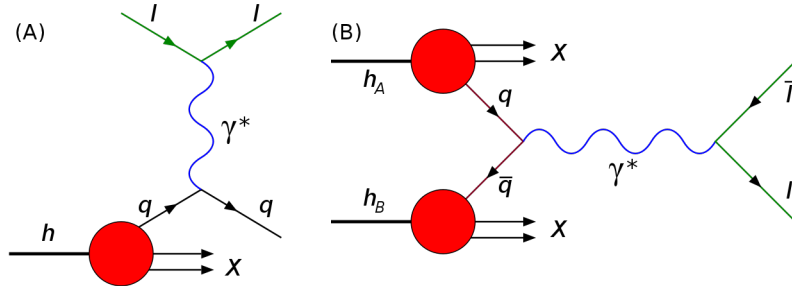


Figure 2.1: (A) Deep inelastic scattering (DIS) is a  $t$ -channel interaction which uses the emission of a virtual photon to probe the target hadron. (B) The similar Drell-Yan (DY) process, using the  $s$  channel version of the DIS interaction, via annihilation of a beam quark with an anti-quark from the target hadron.

As useful as this has been, DIS is only sensitive to momentum and charge of the partonic structure.

In 1970, S. Drell and T.M. Yan were the first to study the process in which high-mass lepton production occurs as a result of inelastic hadron-hadron collisions [3]. This so-called "Drell-Yan" (DY) process is identified to be the result of a quark-antiquark annihilation into a virtual photon which then decays into a lepton pair.

This process, as you see in Figure 2.1, is the  $s$ -channel counterpart to DIS's  $t$ -channel process. Similarly Drell-Yan can give a complementary view of the nucleon's parton distribution. The differential cross section that we will be using is in terms of the fractional momentum variables,  $x_1$  and  $x_2$ , which represent the fraction of the respective hadron's momentum carried by the beam quark and target anti-quark, respectively.

To begin, we start with the annihilation cross section for  $e^+e^- \rightarrow \mu^+\mu^-$  and simply add a color factor of  $\frac{1}{3}$  since only like flavor-antiflavor quarks will annihilate, and use the charge  $e_i^2$  for quark flavor  $i$  [4]. Other

variables referred to in Eq 2.1 and 2.2 and more are defined in Table 2.1.

$$\frac{d\hat{\sigma}}{dM} = \frac{8\pi\alpha^2}{9M} e_i^2 \delta(\hat{s} - M^2) \quad (2.1)$$

The hadronic Drell-Yan differential cross section can be obtained from this by the convolution of the above cross section with the quark distributions in the beam and target.

$$\frac{d^2\sigma^{DY}}{dx_1 x_2} = \frac{8\pi\alpha^2}{9sx_1 x_2 K(x_1, x_2)} \sum_i e_i^2 [q_i^b(x_1) \bar{q}_i^t(x_2) + \bar{q}_i^b(x_1) q_i^t(x_2)] \quad (2.2)$$

Variable	Description
$\alpha$	The fine structure constant
$K(x_1, x_2)$	High-order QCD correction term
$\sqrt{s}$	The center of mass energy of the hadronic collision
$\sqrt{\hat{s}}$	The center of mass energy of the $q\bar{q}$ collision
$Q^2$	The four-momentum of the intermediate time-like photon, squared
$q_i^{t/b}(x)$	The quark number density in the nucleon of the target/beam

Table 2.1: Kinematic variables relevant to the Drell-Yan process .

In addition to the leading-order DY term, there are high-order QCD corrections to consider. These have been studied and accounted for up to  $O(\alpha_s)$  and  $O(\alpha_s^2)$ . These include contributions from high-order  $q\bar{q}$  annihilation ( $q\bar{q} \rightarrow \gamma^* + g$ ) and gluon Compton scattering ( $q + g \rightarrow \gamma^* + q$ ) as seen in Figure 2.2 [4]. The cumulative effect is denoted in the cross section as the  $K(x_1, x_2)$  factor, which can vary between 1.6 and 2.8. For our  $x_1$  and  $x_2$  range,  $K \sim 1.6$ .

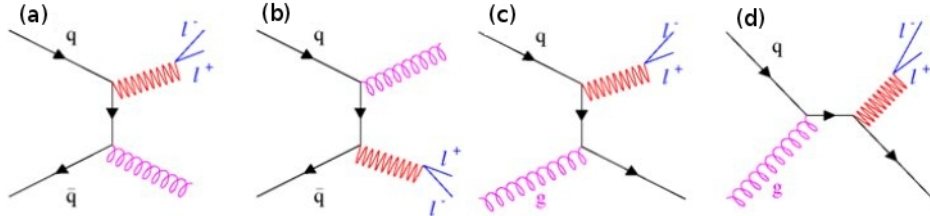
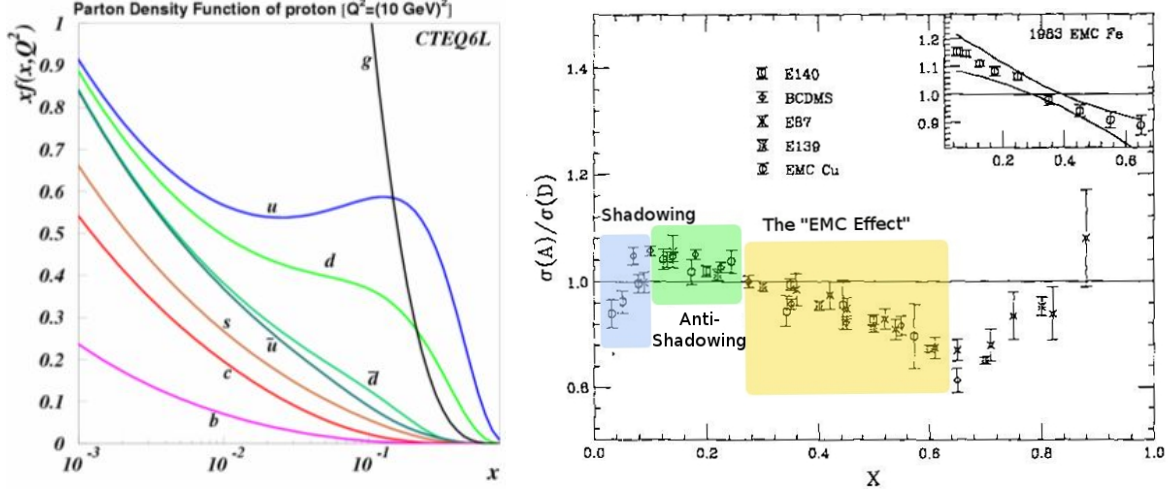


Figure 2.2: The Drell-Yan process has a large range of higher-order QCD corrections that need to be accounted for. (A) and (B) are high order  $q\bar{q}$  annihilations, and (C) and (D) are gluon "Compton scattering" terms.

Now the question is: what can the Drell-Yan process tell us that the well-exercised DIS scattering cannot? The core answer to that is that DIS is not intrinsically sensitive to flavor, whereas DY is. However, to answer the question fully, we must discuss the distribution of quarks in a nucleon.

Let's say that we have two hadrons A and B colliding; a parton of type  $a$  ( $u, d, s, g$ , etc.) comes from A and carries with it a fraction of A's momentum ( $x_A$ ). The same goes for hadron B; a parton of type  $b$  comes





(a) The parton distribution function describing the momentum carried by different types of quark in the proton. (b) The ratio of cross sections (per nucleon) as a function of the target's fractional momentum,  $x_2$ . The EMC Effect region,  $0.3 < x_2 < 0.6$  is the phenomenon discussed here.

Figure 2.3: The proton's momentum distribution and the EMC Effect, with key regions highlighted.

from B and carries momentum fraction  $x_B$ . Now, the probability of finding the discussed parton from A is given by  $f_{a/A}(x_A)dx_A$ . Likewise, the probability of finding the discussed parton from B is  $f_{b/B}(x_B)dx_B$ .

These *structure functions*,  $f_{a/A}(x)$  are called the *parton distribution functions* (PDF's), and they have been the focus of a great deal of experiments over the years by several collaborations. Due to the complex nature of lattice QCD, these PDF's are determined empirically, with only a few rules based in theory. It is important to note that there is normally a  $Q^2$  dependence of these PDF's. At high enough  $Q^2$ , as it is in the case of our experiment, the PDF's no longer scale with  $Q^2$  [12]. That is, for a given  $x$ , the PDF is independent of  $Q^2$ .

An important metric to observe is the probability that a parton  $a$  carries a momentum fraction  $x_A$  in its hadron  $A$ . This can be represented by the following expression:  $x_A f_{a/A}(x_A)dx_A$ . For Drell-Yan interactions in the study proposed here, we are interested in the momentum distribution amongst the quarks in the proton. The CTEQ collaboration has collected data from many experiments, yielding the model represented in Figure 2.3a [11].

Looking to Figure 2.3a we see that at  $x > 0.1$ ,  $u$  and  $d$  quarks dominate  $\bar{u}$  and  $\bar{d}$  quarks. This is key, because this means that, for SeaQuest where we have high  $x_1$  and lower  $x_2$ , the Drell-Yan process is probabilistically dominated by a quark from the beam annihilating with an antiquark from the target. All antiquarks that exist in the target nucleons must come from what are called the *sea quarks*, or the virtual  $q\bar{q}$  pairs that pop in and out of existence amongst the gluons and valence quarks.

As we will discuss in the next section, partons in a bound nucleon behave differently than partons in a free

nucleon. By studying Drell-Yan in nuclear targets, we can investigate the degree to which this modification is the result of a modification to the quark sea.

### 2.3.1 The Drell-Yan Cross-Section

### 2.3.2 Drell-Yan Kinematics

## 2.4 The EMC Effect

The European Muon Collaboration, in 1983, measured the DIS cross section per nucleon ratios of  $Fe$  to  $D$  over a large kinematic range. The result, as seen in the top right of Figure 2.3b came as quite a surprise. It was revealed that the structure function of a nucleon bound in a nucleus differs fundamentally from that of a free nucleon [2]. This difference was not a simple or small effect either; the cross section per nucleon of a nucleus showed to be smaller than that of deuterium at very low  $x_2$ , greater than deuterium at  $0.1 < x_2 < 0.2$ , and then steadily less than deuterium for  $0.2 < x_2 < 0.6$ .

This complex, unexplained behavior opened up a new field of research and theoretical work. Following suit, the different aspects of this nuclear modification garnered some common nicknames. The region where  $x_2 < 0.1$  became known as "*Nuclear Shadowing*", the transition region of  $0.1 < x_2 < 0.2$  is known as "*Anti-shadowing*", and the linear decline in the ratio of cross sections between  $0.2 < x_2 < 0.6$  is generally referred to as the "*EMC Effect*" [7].

The phenomenon was simple – DIS off of a bound nucleon was not the same as off of a free nucleon – but hundreds of theoretical papers were written attempting to explain it away, from multiquark ( $6q$ ) clusters to the exchange of virtual pions in the nucleus. Some have joked that EMC should stand for "*Every Model is Cool*". The focus of recent work (and this paper) is on the "EMC Effect" region, characterized by the distinctly linear downward slope.

Recent experiments at Hall C at JLab and SLAC suggest the following regarding the EMC Effect [12]:

- It is  $Q^2$ -independent
- It's  $x$ -dependent shape is universal (across various nuclei)
- The magnitude (slope) of the effect varies with  $A$
- It thereby might be related to nuclear density

In parallel to this effort, many researchers were working on high-momentum nucleons and short range correlations (SRC's), neither aware yet of their common ground.

# Chapter 3

## Apparatus

SeaQuest is the operational name of Fermilab Experiment #906 (*E-906*) performed at its Neutrino-Muon (*NM*) experimental area. The experiment was designed to take *high-intensity beam* at relatively *low center-of-mass energy*, provide *good mass resolution*, and allow for *accurate target-to-target systematic normalization*. The apparatus consists of a moving target table, two dipole magnets, 7 hodoscope planes, 24 drift chamber planes, and 4 proportional tube planes. Upstream of the target table (towards the beam source), there is also a Cherenkov counter for beam intensity monitoring and there are several segmented wire ionization chambers (SWIC's) for beam profiling.

### 3.1 Apparatus Overview

SeaQuest is a fixed-target experiment. In this style of experiment, a stationary target is placed in the path of an accelerated beam of particles, as opposed to *collider* experiments where two accelerated beams are directed against each other, in opposite directions. The proton beam interacts with the target material and produces a variety of daughter particles. These daughter particles are tracked through a forward spectrometer and selectively filtered dependent on the purpose of the study.

The tuned and monitored 120 GeV proton beam is sent from the Fermilab Main Injector (MI) where the beam protons strike one of the 7 targets. The high-momentum charged particles that are produced are focused onto the various detectors with the solid iron dipole magnet, FMAG, or NM3S. This solid focusing magnet also sweeps away low-momentum particles and acts as a beam dump / absorber.

The SeaQuest Spectrometer consists of a focusing magnet to bend charged particles into the experiment's acceptance, several tracking chambers that record the positions of charged particles through the length of the spectrometer, and an analyzer magnet to bend the particles between tracking stations. The spectrometer measures particle momenta by recording the bend of each charged particle as it passed through the analyzer magnet, where the magnetic field is known. This is performed by reconstructing the trajectory of a particle in one half of the spectrometer (before the analyzer magnet) and then similarly reconstructing the trajectory

of particles in the other half. If two trajectories can be matched up, then the particle momentum can be extracted by taking the ratio of the magnet’s  $p_T$ -kick to the change in the track’s direction.

The spectrometer geometric design and event triggering selection is optimized to detect oppositely-charged pairs of muons while minimizing the sensitivity to various sources of unwanted backgrounds. Positive identification of muons is achieved by requiring signals in the hodoscopes for known muon “roads” along with requiring signals in the proportional tubes located at the farthest end of the experiment, past an iron wall. Electrons and any hadrons are stopped by the solid iron focusing magnet an iron wall further down, while muons will pass through them unencumbered.

The coordinate system is defined as the following: the  $z$ -axis points along the beam direction, the  $y$ -axis points upwards vertically, and the  $x$ -axis lies along the horizontal direction in such a way that a right-handed coordinate system is formed. The terms *upstream* and *downstream* are often used when referring directions or regions in the experimental hall. *Upstream* often refers to the region of the experiment towards the beam source, while *downstream* refers to everything towards the  $+z$  direction. The origin of the coordinate system was chosen to be the point where the proton beam meets the *upstream*-facing surface of FMAG, the solid focusing magnet.

## 3.2 Main Injector Proton Beam

The Fermilab Main Injector (MI) receives protons that have been accelerated by the Radio Frequency Quadrupoles (RFQ), the Linear Accelerator (LINAC), and the Booster, and it continues to accelerate them from 8 GeV up to the nominal energy of 120 GeV. Along the way, the radio-frequency cavity (RFC) accelerators in the LINAC and the MI “bunches” up the protons such that the beam has its characteristic 53.1 MHz structure. After the period of acceleration, the protons are then ‘scraped off’ slowly with each passing *turn* of the collected proton beam and sent down the Neutrino-Muon (NM) beam delivery line for approximately five seconds of every minute, called a “slow spill”, or just “spill”. Beam is extracted using a resonant process, and the extracted beam retains the 53.1 MHz structure of the Main Injector RFC. Each bunch, or “bucket” of protons is less than 2 ns long and the time between bunches is approximately 18.8ns. The spill structure of the beam is depicted in greater detail in Figure 3.1.

The beam sent to SeaQuest is not uniform in time throughout the spill (in more ways than one). There are beam bunches in the MI that are intentionally left empty so that the abort kickers can ramp to full field during a gap in the beam. There are also bunches left empty to allow the injection kickers to inject 8 GeV protons from the Booster without disturbing bunches of protons already in the Main Injector. Typically,

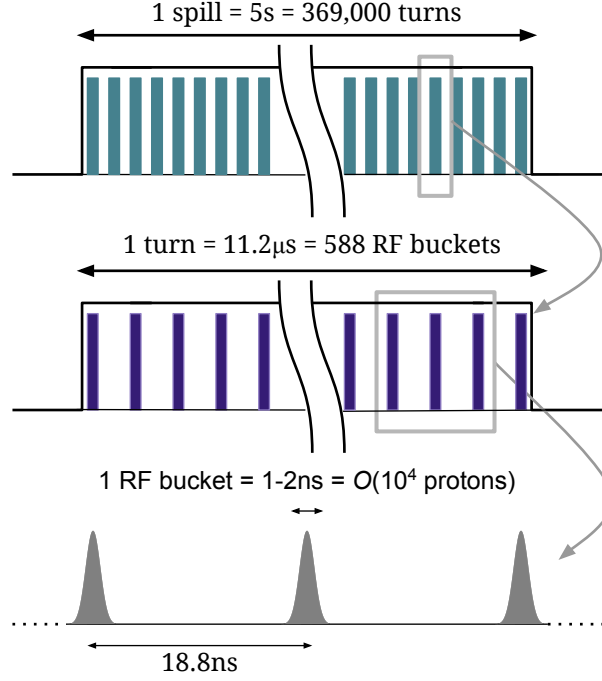


Figure 3.1: Spill structure of the beam delivered to SeaQuest.

498 of the 588 “RF buckets” in the Main Injector contain protons during the SeaQuest slow spill cycle. It is the case, however, for SeaQuest, that the intensity of the bunches corresponding to these 498 full buckets varies greatly throughout the slow spill. On *average*, each bucket will have  $O(10^4)$  protons, and the spill has an intensity of approximately  $2 \times 10^{12}$  protons per second and therefore about  $1 \times 10^{13}$  protons delivered per spill.

Several guiding and focusing magnets bend and deliver beam to the NM beamline which serves both the test beam facility and SeaQuest at NM4. The beam is focused to a width of  $250\mu\text{m}$ . The profile, position, and intensity are measured along the NM beamline by several detectors. The intensity of the beam is monitored by an ion chamber (IC) and a secondary emission monitor (SEM) in the NM3 sector. The beam profile and position are monitored by SWICs and beam-position monitors (BPMs), respectively. The Accelerator Control Network (ACNET) display of the SWIC readout can be seen in Figure 3.2. The closest BPMs and SWICs to the spectrometer were located in NM2 enclosure. The beam profile does not maintain its  $250\mu\text{m}$  shape, and spreads slightly as it moves towards the spectrometer. The final beam profile is measured by inspecting the upstream-facing side of the solid targets, and it was found to be approximately 6mm wide by 1mm high.

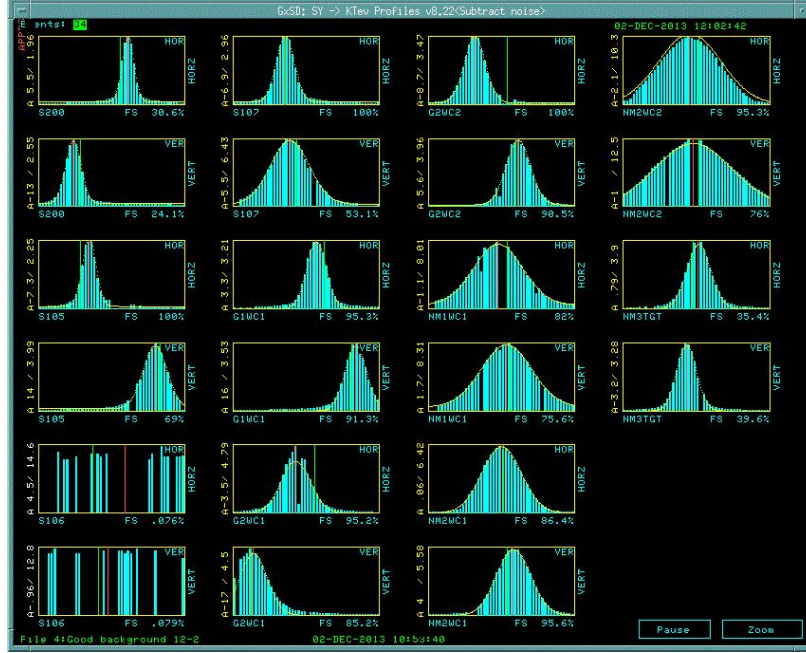


Figure 3.2: Beam profile detailed by SWIC detectors along the NM beam line.

### 3.3 Beam Intensity Monitor

SeaQuest's trigger system (described in detail later) mostly fires on fake dimuons caused by two low  $p_T$  muons from unrelated pion decays. The hits in downstream hodoscopes from the pions combined with hits in the upstream hodoscope from two other unrelated particles frequently add up to a false dimuon signal. Since this type of fake trigger involves four unrelated particles, the probability that a trigger will occur increases with  $I^4$ , where  $I$  is the intensity of the beam bucket, or the number of protons in the triggered beam bunch.

The SeaQuest data acquisition system (also described later in detail) can read out approximately 3000 events per second without significant dead time. During the commissioning run of SeaQuest, the trigger rate was very high and the trigger dead time was close to 100%. These triggers were taken at such high beam intensities that the occupancy of all SeaQuest detector elements was more than 50%, making pattern recognition essentially impossible (see Figure. 3.3). The Beam Intensity Monitor (BIM) was designed to solve this problem.

The SeaQuest Beam Intensity Monitor (BIM) senses when the beam intensity is above a programmable threshold. If an RF bucket with an intensity above this threshold is detected, the BIM sends a signal to inhibit certain triggers until the intensity once more falls below the threshold. The inhibit threshold is tuned frequently as trigger and beam conditions change, but the inhibit threshold is typically set at approximately

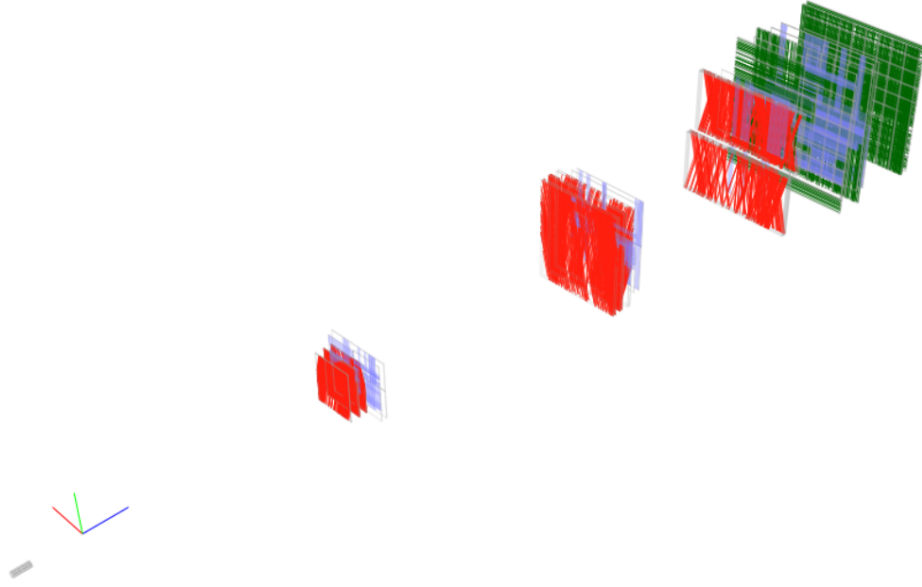


Figure 3.3: A single high-intensity event with majority of all detector elements firing off. Track reconstruction in these cases is impossible.

95,000 protons per RF bunch. For reference, a full RF bucket at an intensity of  $2 \times 10^{12}$  protons per spill is  $\approx 10,000$  protons.

The beam intensity is measured using an atmospheric pressure gas Cerenkov counter. A gas mixture of 80% Argon and 20%  $\text{CO}_2$  is used as the Cerenkov radiator. The counter and readout electronics were designed to have  $O(ns)$  time resolution, and a linear response over a large dynamic range. A diagram of the counter is shown in Figure 3.4. A 45 degree aluminized Kapton mirror directs light to a single photomultiplier tube. A *baffle* of black construction paper held parallel to the mirror ensures that the proton path length through the light-radiating gas with respect to the mirror is independent of beam position. A two-inch diameter 8-stage photomultiplier tube (PMT) is positioned close to the mirror so that all Cerenkov light created between the baffle and the mirror falls directly on the aperture of the PMT. It was observed during the commissioning run that after exposure to  $\approx 3 \times 10^{17}$  protons ( 3 weeks of uninterrupted usage), the mirror reflectivity is significantly reduced in the beam spot, and the mirror then needs to be replaced.

The signal from the BIM is integrated and digitized using a custom charge (Q) integrator and encoder (*QIE*) integrated circuit board, which comes from a family of circuits used first by the KTeV experiment at Fermilab[15]. The chip is clocked with the Main Injector RF clock and provides an ADC (analog-digital conversion) every 18.8ns clock cycle. The light incident on the photomultiplier tube is attenuated using

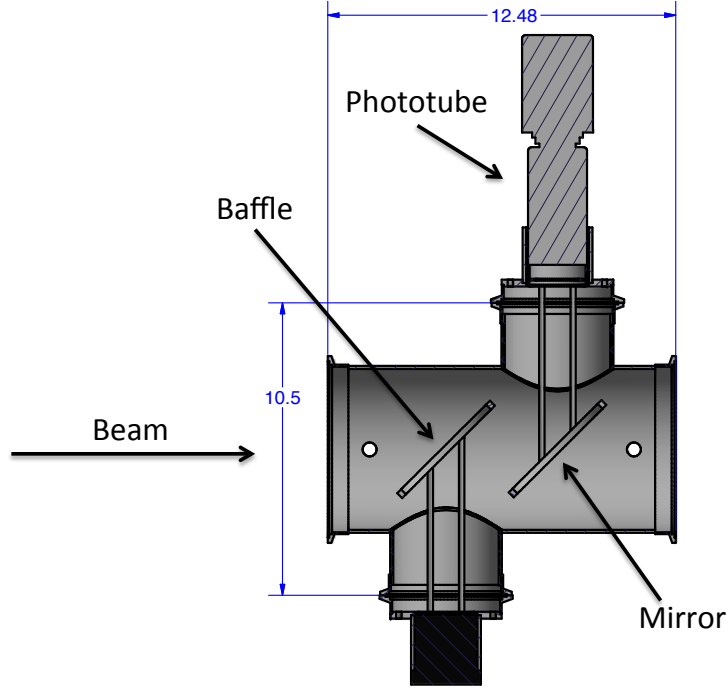


Figure 3.4: The Beam Intensity Monitor (BIM) Cerenkov counter. Measurements are in inches.

neutral density filters (NDF's) so that the QIE least count corresponds to  $\sim 30$  protons per beam bunch.

In addition to inhibiting triggers during high-intensity periods of beam, the BIM readout module also provides critical information used to calculate the number of protons incident on the SeaQuest targets while the experiment is ready and able to trigger. This value is needed to normalize SeaQuest cross section measurements. The BIM readout module provides the following:

- Sum of all ADC signals for the entire spill (QIESum).
- Sum while inhibit is asserted at trigger logic.
- Sum during trigger dead time.
- A snapshot of beam intensity 16 buckets before and after the triggered RF bucket

These are used to calculate a ratio of protons that were 'live' (the experiment can trigger) via the following:

$$liveRatio = \frac{QIESum - (inhibit\ sum + dead\ time\ sum)}{QIESum} \quad (3.1)$$

$$liveProton = totalProton \cdot liveRatio \quad (3.2)$$



where “totalProton” is the intensity value recorded from the SEM detector located just upstream of the BIM Cerenkov counter. The SEM itself is calibrated by foil activation. The snapshot of the triggered RF bucket intensity along with the 32 surrounding RF bucket intensities is used for studies and corrections of the rate-dependent effects on detector efficiencies and reconstructed measurements.

### 3.4 The SeaQuest Targets

A wide range of atomic weights (from 2 to 184) is required to do an A-dependence study of the Drell-Yan process. At SeaQuest, the targets used are  $^1H(\ell)$ ,  $^2H(\ell)$ ,  $C$ ,  $Fe$ , and  $W$ . In addition to the two liquid targets and the three solid targets, two positions on the target table were used for measuring background signal rates: an empty flask, identical to the flasks used for the  $^1H$  and  $^2H$  targets, and a single empty solid target holder. Colloquially speaking: the  $^1H$  target is interchangeably referred to as the liquid hydrogen target,  $\ell H_2$ ,  $LH_2$ , or  $H_2$ ;  $^2H$  is likewise referred to as the liquid deuterium target,  $\ell D_2$ ,  $LD_2$ , or  $D_2$ ; the empty flask is referred to as the “Empty” target; the empty solid target holder is referred to as the “None” target.

These are all mounted on a laterally-moving, remotely positionable table (in the  $\pm x$  direction), able to move over a range of 91.4cm. The table’s center is located at  $(0, 0, -1.25)$  meters, directly in front of the upstream face of FMAG, the solid iron focusing magnet. Because of the  $\sim 5.0$ cm diameter of the targets and the 6x1mm dimensions of the beam, the targeting efficiency was 100%. The details of the target materials are summarized in Table 3.1, and the layout of the target table can be seen in 3.5.

The  $H_2$  gas used is “Ultra High Purity 5.0 Grade” or 99.999% pure. The deuterium has come from two different sources. The first of these is Fermilab-provided supply of gas left over from previous bubble chamber experiments. This gas was known to have a small hydrogen contamination and was measured by mass spectroscopy to have a composition of 85.2%  $D_2$ , 12.7%  $HD$ , 1.2%  $^4He$ , and 0.8%  $H_2$  by mole. As analysis of experimental data commenced, handling the ramifications of the  $D_2$  impurity came under focus. Unexpected bottle-to-bottle variation in contamination became evident, and the sample-taking methodology itself for spectroscopy became suspect of introducing contamination. In order to no simplify analysis and reduce the substantial complexity and cost of further gas analysis, SeaQuest switched to commercially available “Research Grade”  $D_2$ , which is better than 99.6% pure with virtually all  $HD$  to balance. The data analyzed in this paper deals with the impure  $D_2$  target material before this switch. Further information on the  $D_2$  composition and how it is handled in analysis will be covered in Chapter 4.

Each of the three solid target positions is divided into three disks of 1/3 the total thickness provided in

Position	Material	Density [g/cm <sup>3</sup> ]	Thickness [cm]	Interaction Length	Spills/ Cycle (%spills)
1	$H_2$	0.07065	50.8	0.06902	10 (43%)
2	Empty	NA	NA	0.0016	2 (9%)
3	$D_2$	0.1617	50.8	0.1144	5 (22%)
4	None	NA	NA	0.0	2 (9%)
5	Iron	7.874	1.905	0.1135	1 (4%)
6	Carbon	1.802	3.322	0.0697	2 (9%)
7	Tungsten	19.30	0.953	0.0958	1 (4%)

Table 3.1: Characteristics of the seven SeaQuest target positions. The “Spills/Cycle” is only a typical configuration and can vary according to needs and running configurations. The non-zero interaction length of the empty flask is due to the  $51\mu\text{m}$ -thick stainless steel end-caps of the flask and the  $140\mu\text{m}$ -thick titanium windows of the vacuum vessel that contains it.

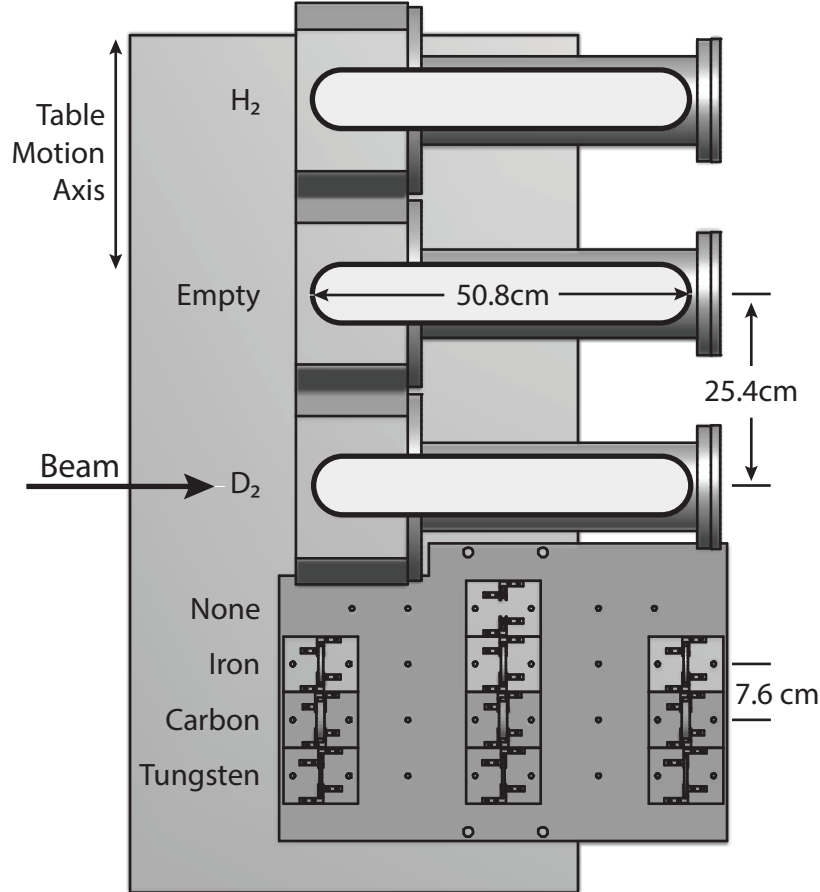


Figure 3.5: The layout of the target table and its seven target positions, as seen from above.

Table 3.1. These disks are spaced 25.4cm apart to approximate the distribution of the liquid target, thereby minimizing target-dependent variation in spectrometer acceptance. The one exception to this is that during the Run II period the iron plugs were more closely spaced (17.1cm). The decision to place these iron disks closer together than the rest during Run II is still unclear.

The target table is able to move between two different targets in about 30 seconds. This allows a change in target in the 55 seconds between successive spills. With this frequent target interchange, the systematic uncertainties associated with drifts in beam characteristics, monitor gains, and detector efficiencies are reduced to a minimum when investigating A-dependent ratios. How much beam time each target received is determined by interaction lengths of the targets along with the amount of statistics desired for certain targets. As the flagship measurement of SeaQuest is the  $\bar{d}/\bar{u}$  asymmetry, more emphasis was placed on the hydrogen and deuterium than the nuclear targets. The spills per cycle and beam time allocation can be found in Table 3.1.

### 3.5 Focusing and Analyzing Magnets

Two large dipole magnets are used in the experiment to select forward going ( $x_F > 0$ ) dimuons, reject low-momentum particles, and analyze their kinematic characteristics. The most upstream magnet, denoted “FMAG”, is a solid iron A-frame magnet with an aperture of 1.22m in the  $x$ -direction and 66cm in the  $y$ -direction. It is assembled from 43.2cm x 160cm x 503cm iron slabs, as shown in Fig. 3.6. The magnet has no air gap, and the iron has extremely high purity, allowing a 2000A excitation current to generate a nearly constant, central magnetic field of 1.9 Tesla (yielding a 2.91 GeV/c total magnetic deflection). The field is generated by exciting the embedded aluminum “*bedstead*” coil to 2000 Amps at 25 Volts (50 kW). The current exciting FMAG is monitored by the Fermilab ACNET system and is broadcast to the SeaQuest slow data acquisition system every acceleration cycle. The excitation is also input to the beam-disabling safety system in order to prevent beam from hitting the SeaQuest spectrometer when FMAG is not fully powered. FMAG also acts as the beam dump for the 120 GeV beam. There is a 5cm diameter by 25cm deep bore drilled into the upstream end of FMAG (recall, this is the origin of the experiment’s coordinate system). The 120 GeV protons that do not interact in the SeaQuest targets 125cm upstream of FMag, interact in the central iron slab. Most of the 2.0 kW beam power is dissipated in this slab and is eventually conducted to the coils and external surfaces to be radiated away.

The downstream magnet, denoted “KMAG”, is a 300cm long iron rectangular magnet with a 289cm wide by 203cm high central air gap. It was originally constructed by the KTeV collaboration [?] at Fermilab.

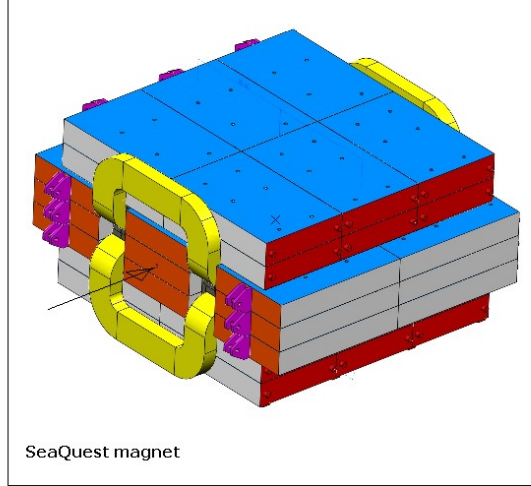


Figure 3.6: Perspective drawing of FMAG’s aluminum coils embedded in an arrangement of iron slabs.

It is excited to a central field of 0.4 Tesla (0.402 GeV/c magnetic deflection) by 1600 Amps at 270 Volts (430kW). The spatial distribution of the magnetic field in K MAG was measured by the KTeV group and re-verified by SeaQuest. In normal running conditions, both F Mag and K MAG bend muons horizontally in the same direction. This two-magnet configuration is often referred to as a focusing spectrometer.

The 2.91 GeV/c and 0.402 GeV/c magnetic deflection delivers a transverse-momentum ( $p_T$ ) kick along the  $\pm x$  direction to charged particles passing through the spectrometer. The magnets bend the paths of the muon in the  $\pm x$  direction, with the sign depending on the orientation of the magnetic fields and the particles’ charges. Between Run II and Run III of data taking, the current direction was reversed, thereby reversing the direction of the magnetic fields. During Run II, the magnetic fields were pointing in the  $-y$  direction, and in Run III, the magnetic fields were flipped to point in the  $+y$  direction. This was done for two reasons: (1) to identify any left-right asymmetries in the experiment, and (2) to limit the amount of radiation on the electronics in the experimental hall, as the large amount of positive particles were being swept directly towards the electronics racks during Run II.

### 3.6 Beam Dump, Shields, and Absorbers

In order to prevent damage to the downstream detectors from the beam and reduce signals from incidental radiation, the spectrometer is designed with a beam dump and two hadron absorber walls. Approximately 125cm downstream of the target table is the water-cooled beam dump whose upstream face is located at (0.0, 0.0, 0.0) m. The beam dump is one of the many solid iron 5m blocks that fill and surround the FMAG coils. The whole length of the beam dump along the beam axis is equivalent to  $\approx 35$  nuclear interaction

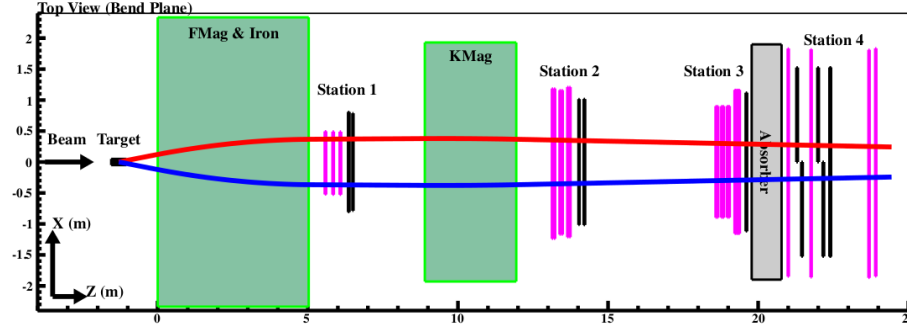


Figure 3.7: Spectrometer layout of FMAG, KMAG, and Detector Stations 1-4.

lengths of iron.

Between the downstream face of FMAG and Station 1, there is a 2 cm thick wall of borated polyethylene which is put in place as a fast neutron shield. This material is 5% boron by weight, with the rest being polyethylene. The polyethylene contains high hydrogen content, making it an effective fast neutron radiation shield, slowing down the fast neutrons down to thermal speeds. The boron in the material provides attenuation of thermal neutrons, thus reducing the levels of capture-gamma radiation elsewhere in the experiment. Borated polyethylene at this thickness is a common and optimal neutron shielding material for areas of low to intermediate neutron flux where the temperature is below  $82^{\circ}\text{C}$  *[citation needed]*. These conditions make the downstream side of FMAG ideal for its placement.

Farther downstream, there is another hadron absorber wall located between Station 3 and Station 4. The absorber wall consists of a stack of 98cm thick iron blocks. This is an equivalent of  $\approx 6$  nuclear interaction lengths. The purpose of this wall is to identify muons at the rear of the apparatus by effectively blocking all other types of particles. The only charged particles which can penetrate this absorber wall are muons.

### 3.7 Tracking Detectors

The tracking detectors are the instruments used for measuring the values of the kinematic variables of the dimuon pairs. Several different types of detectors are grouped together to form a detector *Station*. The types of detectors used are hodoscopes, wire chambers, and proportional tubes. There are four stations throughout the experimental hall that provide tracking information at different points along the spectrometer, numbered from 1 to 4 in order of increasing  $z$ . Station 1 is located between FMAG and KMAG. Station 2 is located at the downstream face of KMAG. Station 3 and 4 are just upstream and downstream, respectively, of the iron absorber wall. The Station layout can be seen in Fig. 3.7

### 3.8 Triggering Hodoscopes

Hodoscope arrays are located at each of the four detector stations. These detectors’ primary usage is to select events with two opposite-signed muon tracks in them. Certain ‘roads’ through the spectrometer are defined in the fast trigger logic, and when two desired roads are observed in a given event, the trigger system tells the data acquisition systems to record that event’s data. In addition to this, the hodoscopes provide analysts with the ability to discard or ignore certain hits in adjacent chambers for which there is no corresponding nearby hodoscope hit. This is useful in decreasing the hit multiplicities in the wire chambers, which in turn decreases the combinatoric complexity of reconstruction algorithms.

Each of the eight hodoscope planes are split into two halves: top and bottom in the case of planes with vertically-oriented paddles, or left and right for planes with horizontally-oriented paddles (denoted by ‘T’, ‘B’, ‘L’, and ‘R’, respectively). A single hodoscope detector element is composed of plastic scintillator material connected to Philips XP 2008 photomultiplier tubes (PMT) by plexiglass light guides. Stations 1, 2, and 4 each have two hodoscope planes, with planes of both vertically- and horizontally-oriented paddles (for measuring in  $x$  and  $y$ , respectively). Station 3 only has vertically-oriented plane, and thus measures in the  $x$ -direction only, which is in the experiment’s  $x - z$  bend plane. The hodoscope planes are named according to detector station and the direction that they measure. For example, the  $y$ -measuring hodoscope plane in Station 2 is called “H2Y”. The individual half-planes are named according to detector station and which half it is of the two. For example, the top half of the  $x$ -measuring hodoscope plane in Station 1 is referred to as “H1T”. The detailed specifications of each hodoscope plane are given in Table 3.2. A precise alignment of the hodoscopes was achieved by examining the distributions of positions of tracked muons at each hodoscope plane when a given hodoscope element in that plane was fired.

Detector	Width [cm]	Overlap [cm]	# of paddles (per half-plane)	Width (x) $\times$ Height (y) (per half-plane) [cm] $\times$ [cm]	$z$ -position [cm]
H1X	7.32	0.3175	23	$162.01 \times 69.85$	666.17 (T), 668.08 (B)
H1Y	7.32	0.3175	20	$78.74 \times 140.12$	653.23 (L), 654.83 (R)
H2X	13.00	0.3175	16	$203.24 \times 152.00$	1,421.21 (T), 1,420.90 (B)
H2Y	13.00	0.3175	19	$132.00 \times 241.29$	1,399.88 (L), 1,405.84 (R)
H3X	14.59	0.3175	16	$227.52 \times 167.64$	1,958.82 (T), 1,958.19 (B)
H4X	19.65	0.3175	16	$304.52 \times 182.88$	2,234.02 (T), 2,251.15 (B)
H4Y1	23.48	0.3175	16	$152.40 \times 365.80$	2,130.27 (L), 2,146.45 (R)
H4Y2	23.48	0.3175	16	$152.40 \times 365.80$	2,200.44 (L), 2,216.62 (R)

Table 3.2: Parameters of all hodoscope planes.  $z$ -positions of half-planes are offset slightly due to slight misalignment and/or overlap of half-planes.

### 3.8.1 Overall structure

Each of Stations 1, 2 and 3 is equipped with a drift chamber (DC) to measure the passing  $x$  and  $y$  positions of muons at its  $z$  location. The trajectory of muons are reconstructed with the measured positions, as described later. The DCs at Stations 1 and 2 are called “DC1” and “DC2”, respectively. Two DCs at Station 3 cover the top and bottom halves, and are called “DC3p” and “DC3m” where “p” and “m” stand for “plus” and “minus”.

The basic structure is common to all the chambers. Each DC consists of six planes of sense wires. Wires are aligned in the vertical direction in two planes called “X” and “X’”. Wires are tilted by +14 degrees in other two planes called “U” and “U’”, and by −14 degrees in the other two planes called “V” and “V’”. The wires in the primed planes are offset by half the drift cell size to resolve the left-right ambiguity of drift direction. Every wire plane is flat vertical to the  $z$  axis, and a drift cell is of the box shape. Table 3.3 summarizes the parameters of the DCs. DC1 and DC3m have been upgraded during the data taking, as listed in Tab. 3.4.

The gas mixture for DC1.2 is Argon:CF4:Isobutane:Methylal (68%:16%:13%:3%), with which the drift velocity is larger than  $50 \mu\text{m/ns}$  (i.e. fast gas) and thus the hit-rate tolerance is better. The gas mixture for the other chambers is Argon:Methane:CF4 (88%:8%:4%).

Table 3.3: Parameters of all chambers. Those of primed planes are almost the same as of unprimed planes. The  $z$ -positions of U and V planes are relative to those of X planes.

Chamber	Plane	Number of wires	Cell width (cm)	Width × height (cm)	$z$ -position (cm)
DC1.1	X	160	0.64	$102 \times 122$	617
	U, V	201	0.64	$101 \times 122$	$\pm 20$
DC1.2	X	320	0.50	$153 \times 137$	617
	U, V	384	0.50	$153 \times 137$	$\pm 1.2$
DC2	X	112	2.1	$233 \times 264$	1347
	U, V	128	2.0	$233 \times 264$	$\pm 25$
DC3p	X	116	2.0	$232 \times 166$	1931
	U, V	134	2.0	$268 \times 166$	$\pm 6$
DC3m.1	X	176	1.0	$179 \times 168$	1879
	U, V	208	1.0	$171 \times 163$	$\pm 19$
DC3m.2	X	116	2.0	$232 \times 166$	1895
	U, V	134	2.0	$268 \times 166$	$\pm 6$

### 3.8.2 Performance requirement

The acceptance size of each chamber has been adjusted with a Drell-Yan event simulation in order to be as sensitive as possible to the  $x_2$  range of interest. Particularly the wider the acceptance width is, the higher

Table 3.4: Combination of chambers per data taking period.

Run	Period	Chamber combination
1	2012 Mar.-2012 Apr.	DC1.1-DC2-DC3p-DC3m.1
2	2013 Nov.-2014 Aug.	DC1.1-DC2-DC3p-DC3m.2
3	2014 Nov.-2015 May	DC1.1-DC2-DC3p-DC3m.2
3	2015 Jun.-2015 Jul.	DC1.2-DC2-DC3p-DC3m.2
4	2015 Sep.-2016 X	DC1.2-DC2-DC3p-DC3m.2

the reach in  $x_2$  is.

The position resolution of every single plane is required to be 400  $\mu\text{m}$ . It corresponds to a momentum resolution of  $\Delta p/p$  (%) =  $0.03 \cdot p$  (GeV/ $c$ ). The resolution of dimuon invariant mass is dominated by the multiple scattering in FMag, since the chamber momentum resolution is about 10% of the total mass resolution at maximum. Therefore this requirement is not more strict than the others.

The detection efficiency of every single plane is required to be 95% or more. In the track reconstruction, if a track is required to associate with five planes out of six per every chamber, the reconstruction efficiency of a track is 90%, which is thought to be acceptable.

The hit-rate tolerance is a key feature because the spectrometer is exposed to a large number of background particles. It is particularly significant for the most-upstream station (i.e. Station 1). The hit rate is maximum at the edge of chamber acceptance. As extracted from experimental data, it is 3.0 MHz/wire at DC1, 1.6 MHz/wire at DC2 and 0.7 MHz/wire at DC3 with a beam intensity of  $5 \times 10^{12}$  protons/spill. The gas-amplification gain should not be degraded under these hit rates. The probability of double hits per wire per event should be low enough.

### 3.8.3 Constructions

The DC1.1, DC2 and DC3m.1 chambers have been inherited from E605 (DC2 and DC3m.1) [10] and E866/NuSea (DC1.1) [8, 13], previous Drell-Yan experiments based at Fermilab. Since these chambers haven't been used for decades after the previous experiment, they had to be refurbished by restringing a large fraction (30% of sense wires in these chambers) of broken and loose wires with wires of appropriate tension and by attaching new readout electronics.

The DC3p and DC3m.2 chambers were designed and constructed for this experiment in order to cover the large acceptance required at Station 3. The first part of data taking, Run 1, was carried out with DC3m.1 while preparing for the construction of DC3m.2. As DC3m.2 is wider than DC3m.1 by 25 cm at each side, the anticipated statistics on  $\bar{d}/\bar{u}$  will increase by 20% at  $x_2 \sim 0.3$  and 10% at  $x_2 \sim 0.4$ . The operational stability has been greatly improved; no dead/noisy wire, no HV trip and no leak current.



The DC1.2 chamber was also designed and constructed for this experiment. As it is wider than DC1.1 by 25 cm at each side, the anticipated statistics on  $\bar{d}/\bar{u}$  will increase by ??% at  $x_2 \sim ??$ . In addition, with the smaller cell width it has a better hit-rate tolerance.

### 3.8.4 Electronics

The SeaQuest wire chamber readout system uses a custom amplifier-discriminator integrated circuit called ASDQ designed at U. Penn. for CDF [14]. 8-channel “ASDQ cards” are mounted on each wire chamber. On DC2 and DC3, copper grounding card guides<sup>1</sup> connected to the chamber frames provide both mechanical support and the reference voltage for the ASDQ inputs. Except in DC1.1, all cathode wires are biased with negative high voltage and the anode wire signals are DC coupled to the ASDQ inputs. DC1.1 uses positive HV applied to the anode wires. The signals from these chambers are AC coupled to the ASDQ inputs through high voltage blocking capacitors that are integral to the chambers.

A single twisted pair ribbon cable connects each ASDQ card to a Level Shifter Board (LSB). This cable carries the (differential) discriminated output signals and also the bias voltages for the ASDQ as well as a discrimination threshold voltage and other control voltages. Each LSB services 8 ASDQ cards. Up to 14 LSBs are housed in a 9U crate that distributes 24V power to the LSBs on a narrow backplane. The 24V is provided by a rack mounted linear power supply connected by a cable bundle to the LSB crate backplane. Multiple LSB crates can be serviced by a single power supply. One LSB per station is controlled using an Ethernet interface. Control of the other LSBs at that station occurs using a two pair serial protocol implemented using short RJ11 cables linking one LSB to the next. A test pulse can also be injected to selected groups of channels. The timing of the test pulse can be determined by a TTL pulse distributed to the LSBs using a daisy-chain of LEMO cables, or independently by each ASDQ card being tested.

Eight 17-pair ribbon cables connect eight ASDQ cards to the back side of a single LSB. The LSB converts the differential signals from the ASDQs to standard LVDS. The LVDS outputs are carried on 4 ribbon cables to TDC modules. Typically, one 64-channel LSB is connected to one corresponding 64-channel TDC. The ASDQ/LSB system was designed at Fermilab for SeaQuest.

### 3.8.5 Measurement of Performance

Table 3.6 summarizes the performance of all the DCs. The performance of DC1.2 is of anticipated values based on simulations because DC1.2 is being constructed. Those of the other DCs are of measured values in Run 3.

---

<sup>1</sup>Unitrack “Ground-R-Guide,” see [http://www.unitrack.com/metal\\_card\\_guide-ground-r-guide.html](http://www.unitrack.com/metal_card_guide-ground-r-guide.html).

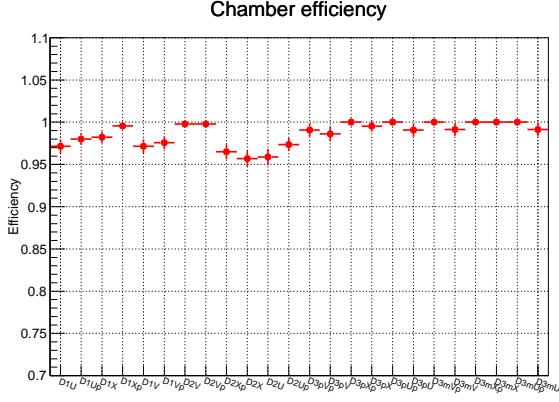


Figure 3.8: Single-plane efficiency. *This plot is NOT final. Should we show those of DC3m.1? Should we use a table instead of plot?*

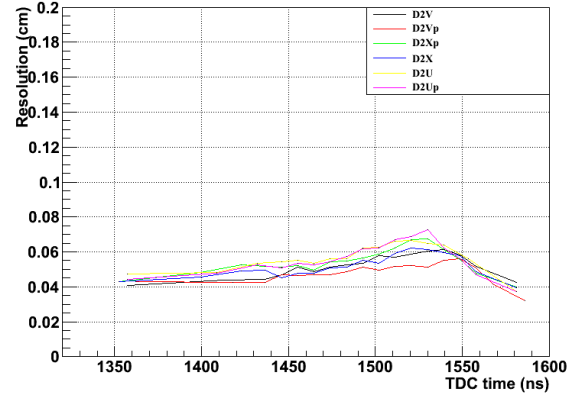


Figure 3.9: Single-plane position resolution. *This plot is NOT final. The horizontal axis has to be converted to drift distance. If the resolution of all chambers/planes is rather constant, we should use a table instead of plot.*

Figure 3.8 shows the detection efficiency of all 18 planes. All planes of DC3p and DC3m.2 are nearly 100% efficient. Several planes of DC1.1 and DC2 are less efficient, because the high voltages of these planes were set lower to prevent occasional power supply trips. All the planes have been proven to meet the requirement. The efficiency of DC1.2 hasn't been measured yet.

Figure 3.9 shows the position resolution of all 18 planes. The resolutions of all planes are on average 500  $\mu\text{m}$ . All the planes have been proven to meet the requirement. The resolution of DC1.2 hasn't been measured yet.

Regarding the hit-rate tolerance, the probability of double hits per wire per event is estimated to be xx% on average, based on the measured hit rate per wire. Analysis techniques to resolve the double hits are being examined.

Table 3.5: Performance of all DCs. That of DC1.2 is of anticipated values based on simulations, and those of the others are of measured values in Run 3.

Chamber	Drift velocity ( $\mu\text{m}/\text{ns}$ )	Maximum drift time (ns)	Position resolution ( $\mu\text{m}$ )	Plane efficiency (%)
DC1.1	30	100	500??	98%??
DC1.2	n/a	n/a	n/a	n/a
DC2	5	200	500??	98%??
DC3p	5	200	500??	98%??
DC3m.1	5	100??	500??	98%??
DC3m.2	5	200	500??	98%??

### 3.8.6 Mass Resolution

The mass resolution of the spectrometer is limited by the resolution of the tracking chambers. First the momentum resolution can be derived from the respective positions of the chambers and the resolutions of the individual chambers:

$$\frac{\Delta P}{P} = \frac{P}{P_{kick}} \sqrt{\Delta r_1^2 + \left(1 + \frac{z_1 - z_2}{z_2 - z_3}\right) \Delta r_2^2 + \left(\frac{z_1 - z_2}{z_2 - z_3}\right)^2 \Delta r_3^2} \quad (3.3)$$

where  $z_n$  is the z-position of the  $n$ th station, and  $\Delta r_n$  is the resolution of the  $n$ th chamber.

There are two other additional factors that contribute to the momentum resolution:

## 3.9 Triggering Matrices

The SeaQuest Trigger System selects candidate dimuon events from the high-rate environment using discriminated hodoscope signals.

### 3.9.1 Requirements

The trigger must select events of interest to the main physics goals with high-enough efficiency to facilitate high-statistics analyses. Therefore, the trigger is optimized to accept high-mass ( $4 - 10\text{GeV}$ ) dimuons originating from the targets. The trigger should intentionally reduce acceptance of dimuons from other, higher-rate sources, such as  $J/\Psi$  decays and dimuons originating from the beam-dump. The overall trigger rate must be kept low enough to maintain an acceptable DAQ livetime. Additionally, the trigger should be internally deadtime-free. The trigger should be capable of firing on any and all RF-buckets while the DAQ is live.

The trigger should be sufficiently flexible to quickly accomodate changes in the spectrometer, beam conditions, and physics goals. Any changes to the geometric acceptance of the spectrometer, whether caused by new/moved detectors, changes in the magnetic fields, or something else, must be immediately reflected in the trigger in order to maintain high-signal efficiency and high background rejection power. Similarly, a change in the beam duty factor or intensity should be accompanied by a change in the trigger acceptance, ensuring trigger rate optimization. Finally, the trigger should be capable of modifying the acceptance to facilitate special runs for other physics goals. For these reasons, the design of the trigger system must allow for significant flexibility in the trigger-imposed acceptance.

Lastly, the design of the trigger system should include self-diagnostic capabilities, allowing for constant

monitoring of the trigger system’s performance. Internal pulser-testing is employed to test the function of each compiled firmware, every time the trigger logic changes. Data from the internal TDCs is used by offline software to check the self-consistency of the trigger for each recorded physics event.

Table 3.6: Performance of all DCs. That of DC1.2 is of anticipated values based on simulations, and those of the others are of measured values in Run 3.

Trigger	Condition	Sign	# $\mu$
FPGA-1	$T \wedge B$ , 3-of-4	$+\wedge-$	2
FPGA-2	$T \vee B$ , 3-of-4	$+\vee-$	1
FPGA-3	T, 3-of-4	$+\vee-$	1
FPGA-4	B, 3-of-4	$+\vee-$	1
FPGA-5	$T \wedge B$ , 3-of-4	Any	2
NIM-1	$T \wedge B$ , 4-of-4	NA	NA
NIM-2	$T \wedge  B$ , X3-X4	NA	NA

## 3.10 Data Acquisition Systems

## 3.11 Data Productions

### 3.11.1 Production Processing

The three raw outputs of the data acquisition systems, as described above are (1) Main DAQ CODA files, (2) Scaler DAQ CODA files, and (3) Beam DAQ ASCII files.

Each raw data file corresponds to the data taken from certain subsystems over approximately one to two hours of running time. These three types require varying degrees of de-serialization, parsing, processing, and storage – a process as a whole defined as *decoding*.

All raw data files are backed up to long-term tape storage (managed by FNAL Computing Division), and the decoded and processed data gets stored on one of four MySQL servers to be used for analysis by the collaboration. Data is also output to a ROOT file for the ease of use of one of the two independent tracking programs.

Contiguous blocks of decoded and tracked data is then grouped together into *merged* productions, available on all MySQL servers, providing collaborators large sets of curated and easily analyzable data.

### 3.11.2 Decoding Raw Data

The CODA file decoding is nearly identical for MainDAQ and ScalerDAQ, and only differ by content; the MainDAQ contains TDC readout. For each one to two hour *Run*, the CODA files can be well-described as

the following sequence of events (and the data they contain):

1. Prestart Event (Run data)
2. Begin Spill Event (Spill data, Scaler readout)
3. Many Physics Events (Event data, TDC readout)
4. End Spill Event (Spill data, Scaler readout)
5. SlowControl Event (Slow control readout, Spill ID readout)
6. Spill Counter Event (Spill ID readout)  
...(Repeat 2-6 for each *Spill*)
7. End Event

Our decoding program uses C and C++ in conjunction with Jefferson Lab's CODA I/O library to read these events and parse them according to their individual formats. Data from these CODA events are decoded and placed into hierarchical categories.

## Run Level Data

Run-level data contains data and metadata pertaining to the entirety of the run that is recorded. At the time of the Prestart Event, the date and time of the run are stored, along with a readout of the specific settings of all non-trigger TDC boards.

After the End Event is encountered, metadata is aggregated and stored regarding such items as the number of chamber hits, the triggers that were fired, the target positions used, average magnet currents, and other useful metrics.

## Spill Level Data

The *Beginning of Spill* (BOS) and *End of Spill* (EOS) events bookend the set of physics events for a given spill. At each BOS and EOS events, the 140 MHz VME scalers are read out. At the beginning of the spill, all scalers should be zeroed out, and then read out again after the spill has ended.

Slow Control events are read out between spills, which contain data regarding the current spill identifier number, target systems, beam and radiation monitors, and environmental readings.

The spill identifier (*spillID*) is what is used to synchronize the data together across various data acquisition systems. As such, the *spillID* is read out redundantly in both Slow Control and Spill Counter events (which contain only the *spillID* value) to ensure that the data is appropriately labeled.

When the End Event is reached, the independently-recorded Beam DAQ data (recorded in an ASCII file) is read and stored with the rest of the Spill-level data.

### Event Level Data

For each spill,  $\sim 3k$  events are triggered to be recorded. With each event, three types of information is stored: the trigger which fired the event, a measure of the beam intensity per RF bucket, and the full detector readouts. The detector readouts require the most processing of all the rest of the data. The CODA files contain the hardware addresses of each detector *hit*, along with a *TDC time*. The following steps briefly summarize the processing steps:

1. Mapping: Map the hardware address to a detector name and detector element number
2. Timing: Classify hits as in-time or not and calculate *drift time* from TDC time
3. R-T (time-to-space): Translate *drift time* to *drift distance*
4. After-Pulse Elimination: Remove hits that result from signal reflection and other electronic artefacts
5. Trigger Road Reconstruction: Use *v1495* TDC hits to reconstruct possible trigger roads that may have fired
6. Hodoscope Masking: Remove drift chamber hits that have no adjacent hodoscope hit
7. Trigger Road Masking: Same as hodoscope masking, but only using hodoscopes from reconstructed trigger roads

This fully processed data is then stored into one the experiment's MySQL databases.

### 3.11.3 Online and Offline Processing

There are two modes of productions: on-line and off-line productions. For on-line productions, all Run- and Spill-level data is decoded, but only 1-in- $n$  Physics Events are processed, where  $n$  is typically 15. This “*sampling mode*” is used in order for the decoding to reliably keep up with even high-intensity beam data.

For off-line productions, a large group of categorically similar runs is defined, and the chain of production processing is initiated. The steps of this process is generally emphdecoding, tracking, archiving, and merging.

The decoding and tracking is performed on Fermilab Computing Service's FermiGrid, which provides the computing resources necessary to process hundreds of runs simultaneously.

A single decoding job submission will output the processed data to one of the four available MySQL servers and also to a ROOT file. Then, one job will be submitted to run one of the two tracking programs on the ROOT file, while another job is submitted to run the other tracking program on the MySQL data.

Once the tracking is completed, the ROOT file and the *Hit* table from the MySQL production is archived on the Fermilab BlueArc NAS backup system for future use, if necessary.

Upon the completion of decoding and tracking of a specified range of runs, all of their Run-, Spill-, and Event-level data, along with its tracked data, is combined into a single *merged* schema. These *merged* schemas are mirrored across all four of the MySQL servers for optimal redundancy and availability.

### 3.12 RDBMS Data Structure

The processed data is primarily stored in MySQL Server 5.1 databases. MySQL is an open-source **R**elational **D**atabase **M**anagement **S**ystem (RDBMS) developed by Oracle that is well-suited for the storage and responsive querying of hierarchical data.

Each run is decoded into its own schema, and contains its own instances of all tables of a specified design. The tables are all *join*-able to each other by sharing *foreign keys* with each other in the form of the *runID*'s, *spillID*'s, and *eventID*'s. The contents of the tables are *indexed* in such a way that *joins* and queries gain a speed performance boost, but this comes at the cost of disk space.

The data on the server is world-wide accessible and can be queried using the standard querying language. The queried data can be directed to any analysis code in any programming language due to the large array of MySQL API's available.

### 3.13 Data Quality

# Chapter 4

## PMT Upgrade

### 4.1 Introduction: PMT Sagging

During Run I of SeaQuest, it was observed on April 17th that there appeared to be a drop in expected performance in the  $y$ -measuring hodoscopes (Figure 4.1). This is assumed to be due to periods of beam reaching the NM3 enclosure being unusually intense. The result of this is pulses of light being channeled to the PMT's at an intensity and/or rate that the PMT is not capable of handling.

The understood cause of this "*sag*" in performance is due to a destabilization in the voltage divider (PMT base) that holds each dynode stage at a specific voltage. When the PMT base destabilizes and is unable to maintain an appropriate voltage difference between dynode stages, this leads to inefficient performance of the PMT.

Here, we assemble a new base for our Philips XP-2008 PMT's, test several variations, and compare its performance to the original PMT base and to some Hamamatsu PMT's.

### 4.2 PMT Base Terminology and Common Characteristics

Each base divides -1500V over the photocathode (K), ten dynode stages (D1-D10), and the anode (A). Some common features.

There are two currents that are discussed in this document are:

- **Signal Current** - This is the signal that passes over the anode, which is the end-result of the cascading secondary emission electrons from each dynode stage.
- **Bleeder Current** - This is the current through the voltage divider. It is termed the "bleeder" current since the compounding electrons in the signal current must be "bled" from the current through the voltage divider.

Throughout these voltage base designs, capacitors are commonly implemented in the latter dynode stages. These capacitors, when charged, are utilized when a large pulse of light induces a large signal current. When



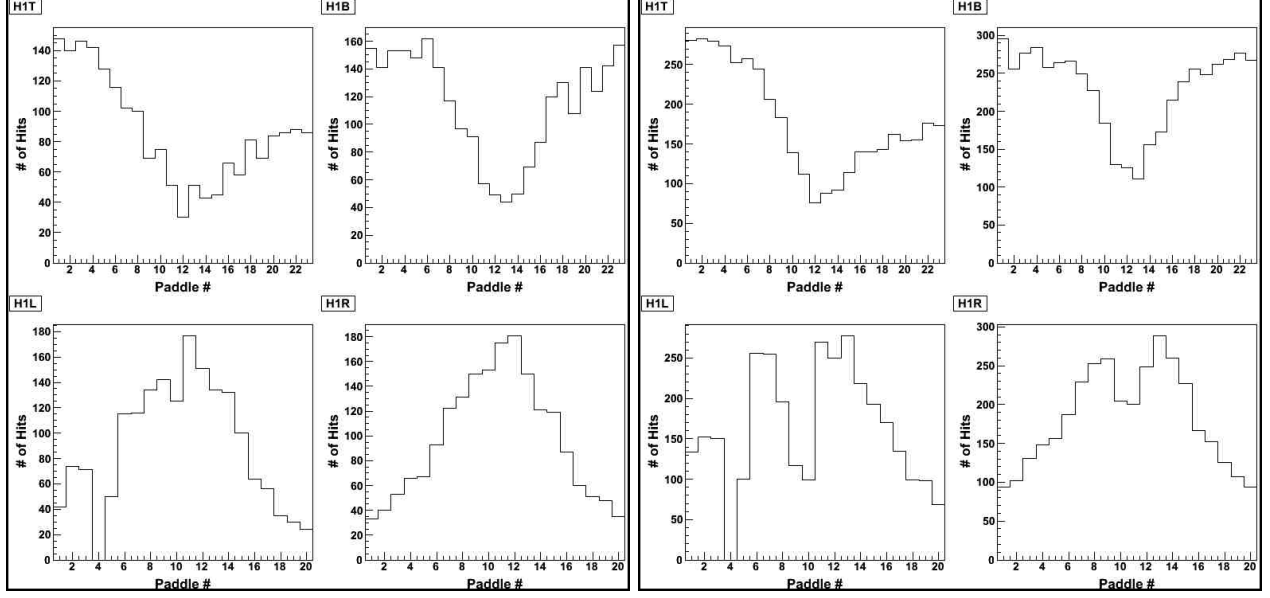


Figure 4.1: (Left) Histogram of hodoscope 'hits' in a typical event; (Right) Histogram of high-intensity event, with marked sagging in the middle of the y-measuring hodoscopes

this happens, the capacitors help to replenish the charge on the dynode stages without requiring the charges to be drawn from the bleeder current, thereby keeping the voltage across the dynode stages more stable.

## 4.3 PMT Base Design Iterations

### 4.3.1 Original Base

This is the PMT base that is currently used with our XP-2008 PMT's. It features capacitors of increasing capacitance along the last six stages, and steadily increases the voltage across the final four stages.

### 4.3.2 Prototype Base v1

This is the base design provided by Sten Hansen (Fermilab Particle Physics Division), designed in 2010 for the same model of PMT's for use at CERN.

Three important features of this design include:

- Lower resistance
- Parallel currents
- Transistors and diodes
- (More) Even distribution of voltage

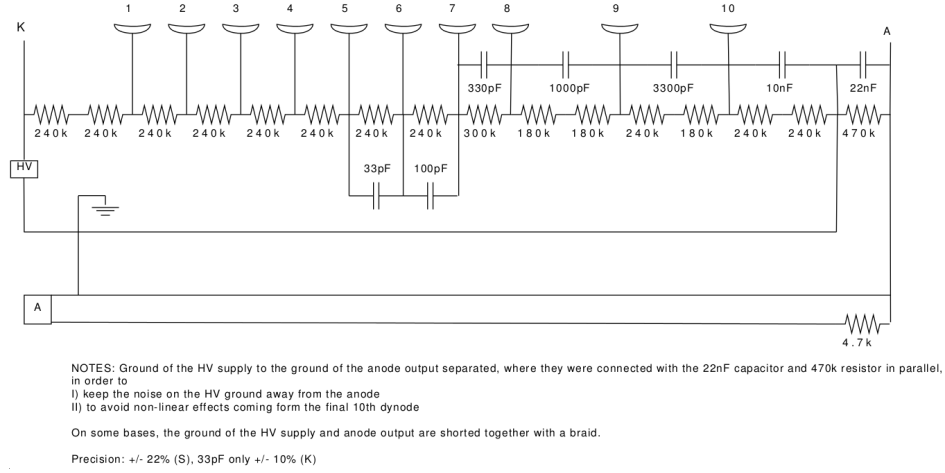


Figure 4.2: The original PMT base design.

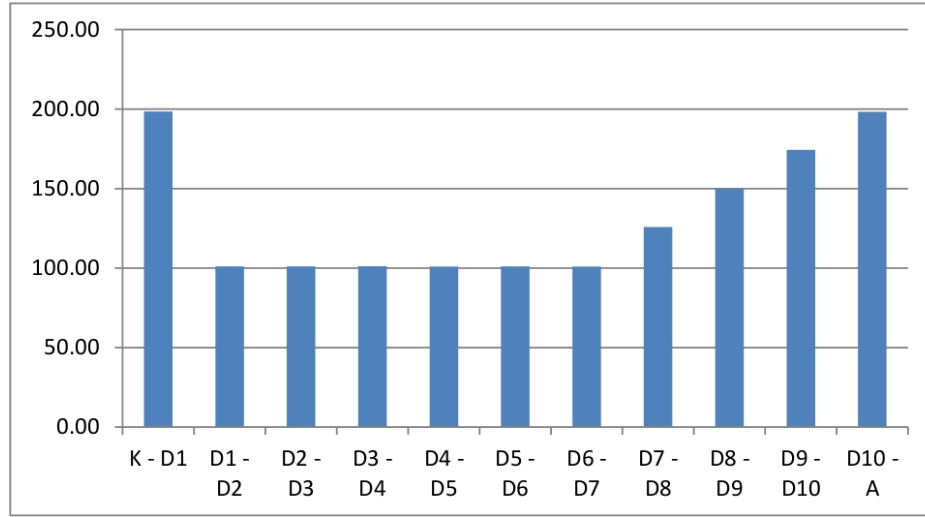


Figure 4.3: The (negative) voltage between subsequent stages for the original PMT base.

The lower overall resistance of the voltage divider increases the bleeder current. This means that the base will be more capable of handling high-intensity/-rate events, as it will be better able to replenish the charges on each dynode stage in the case of a large signal. Typically, the larger the bleeder current, the larger the signal current can be without destabilizing the voltage divider.

At dynode six on Figure 4.4, we see that the current is split into two paths. The intent here is for the smaller current that goes through the series of  $1M\Omega$  resistors maintains the voltage difference, and the larger current that freely passes through the transistors supplies the dynode stages with needed charge.

Transistors are introduced here to maintain the proper voltage division. If at any point the proper voltage drop across the gates of the transistors is not supplied (and thereby across the dynode stages), the source-to-drain current through the transistor is stopped until the proper gate voltage is restored. This helps

to regulate the voltage across the dynodes, but if the charges lost to the signal current are not restored, the PMT will still eventually "sag" and fail.

The diodes are there to prevent the current from moving across the transistors improperly, and thereby preventing them from being damaged when powering the circuit on and off.

Also, the voltage across each stage, from D1 to A, are relatively flat. According to the specifications for the Philips XP-2008 photomultiplier tube, this is the recommended voltage configuration for maximum gain [9].

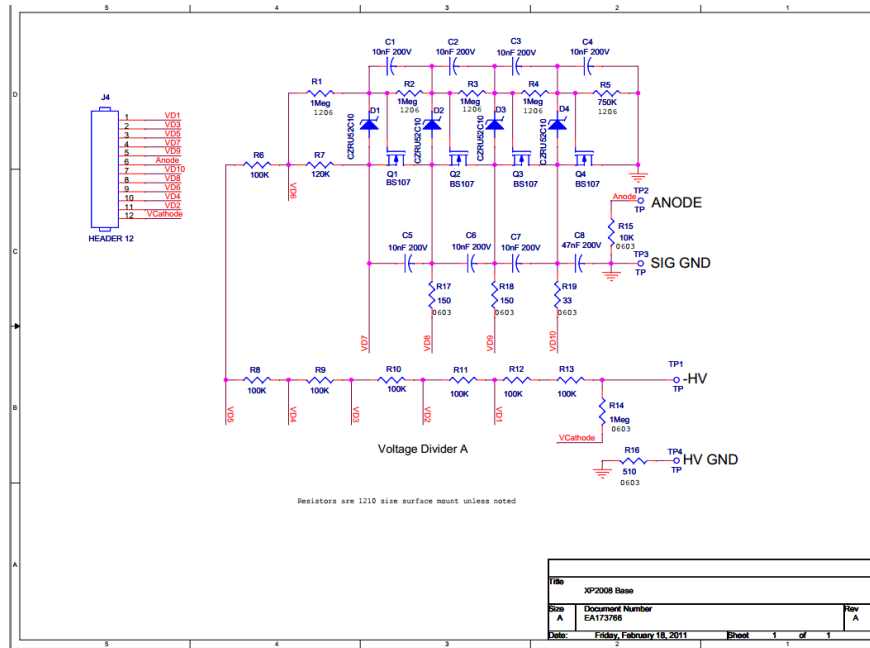


Figure 4.4: The Prototype v1 board.

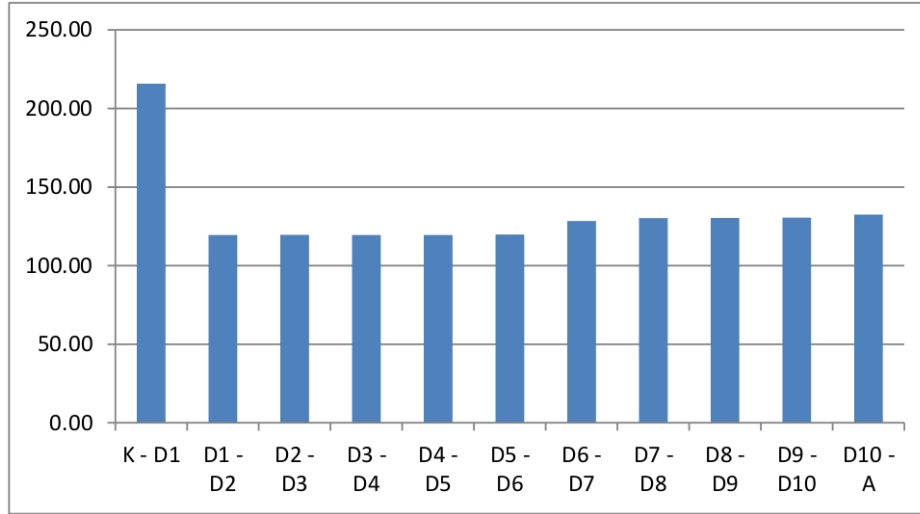


Figure 4.5: The (negative) voltage between subsequent stages for the Prototype v1 PMT base.

### 4.3.3 Prototype Base v2

The first modification made to the prototype board was to simply halve the resistance of each of the first six stages (R6-R13 on Fig. 4.4) to increase the bleeder current.

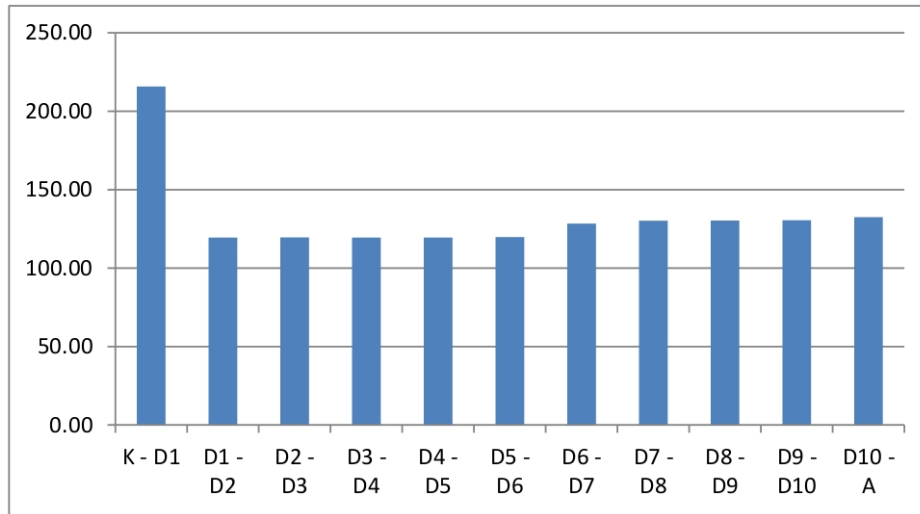


Figure 4.6: The (negative) voltage between subsequent stages for the Prototype v2 PMT base.

### 4.3.4 Prototype Base v3

This modification "transistorized" the D5-D6 and D6-D7 stages in the case that the destabilization was occurring even at these earlier stages (Figure 4.7).

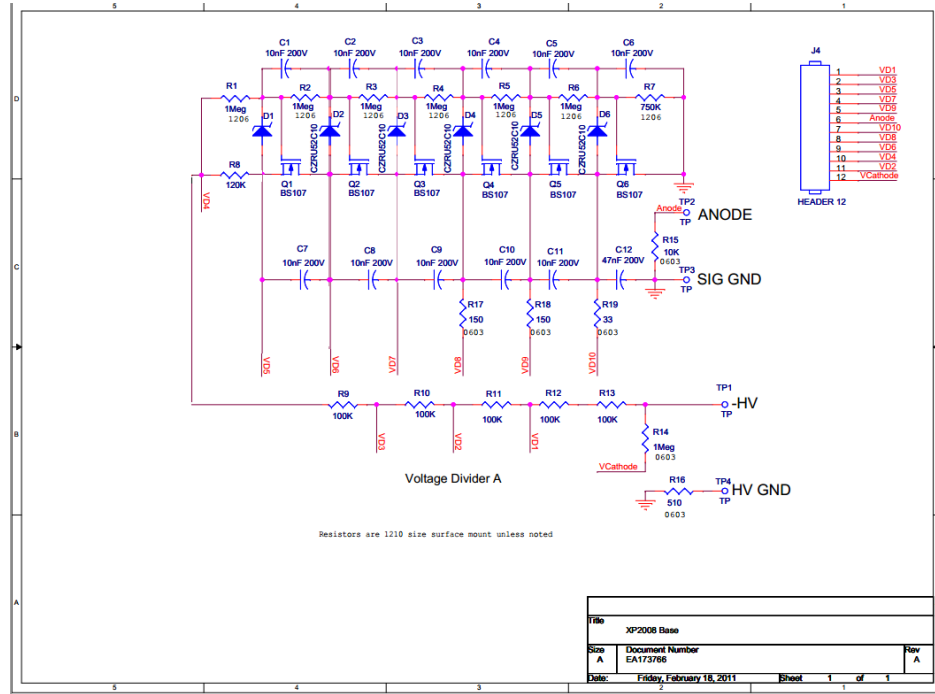


Figure 4.7: The Prototype v3 board: 3 more transistorized stages than the Prototype v1 design.

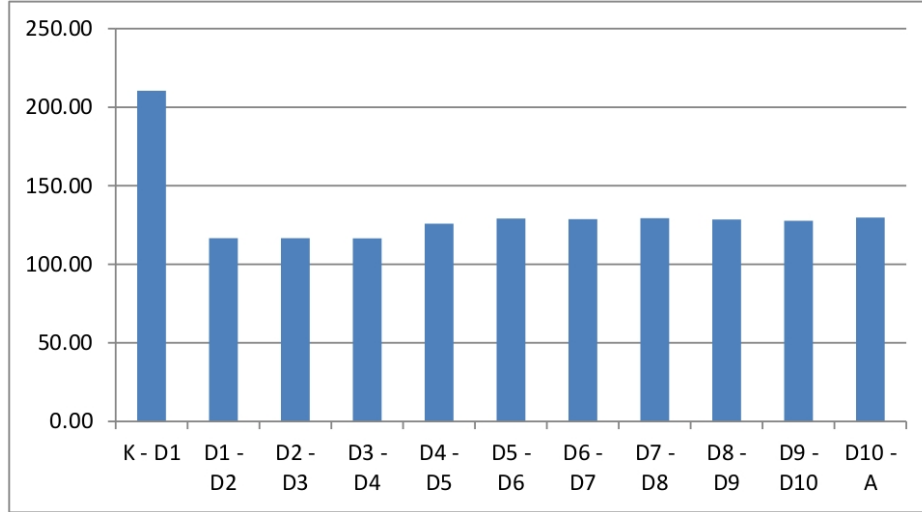


Figure 4.8: The (negative) voltage between subsequent stages for the Prototype v3 PMT base.

#### 4.3.5 Prototype Base v4

Here, the resistance over the final stage (D10-A) was increased from  $1M\Omega$  to  $1.5M\Omega$  (R5 in Figure 4.4). This was done in case that the final batch of electrons needed help being "swept" to the anode with a higher voltage difference.

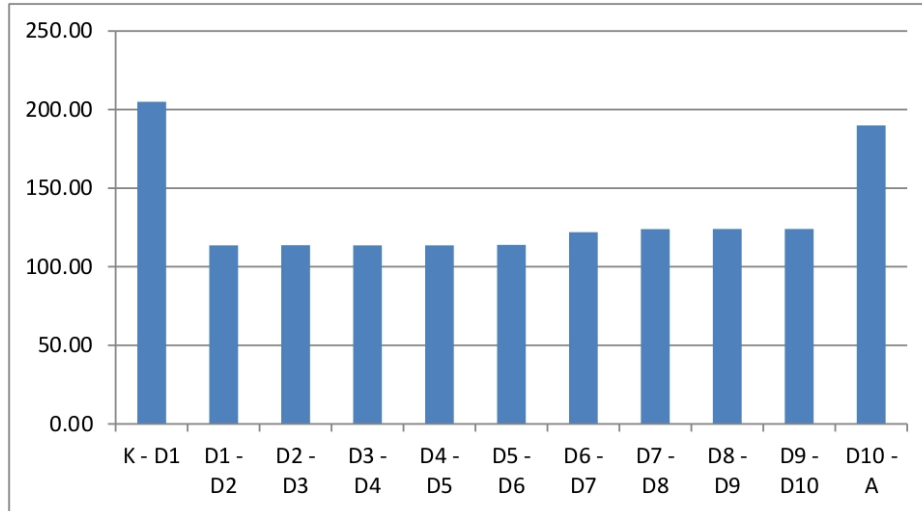


Figure 4.9: The (negative) voltage between subsequent stages for the Prototype v4 PMT base.

## 4.4 PMT Base Comparisons

There is a specific difficulty with the objective to increase the rate capability of our PMT's. This difficulty is that we do not have a target rate to attain. The rate and intensity that caused the original PMT+base to sag is unknown, and if it was known, it would be difficult to match the intensity with an experimental setup.

As a result, the objective in these tests is to *compare* the performance of the same PMT using different bases.

### 4.4.1 Testing Apparatus and Measurements

In this experiment, a PMT attached to a PMT base is placed into a light-tight box along with an fast-pulsing LED.

The LED is driven by an Agilent function generator capable of generating signals up to 30MHz. The LED's intensity is attenuated by a neutral density filter (NDF), with a rating  $D=3.0$ , where the NDF allows 1 in  $10^D$  photons through (1 in 1000 for  $D=3.0$ ).

The PMT base is powered by a high voltage supply with an ammeter between the two in order to measure the bleeder current. The PMT signal is processed



Figure 4.10: Inside of a lightbox, we have our prototype board (left) wired up to a Philips XP-2008 PMT (middle), facing a fast-led source (right)

# Chapter 5

## Analysis

### 5.1 Particle Identification

### 5.2 Data Selection

#### 5.2.1 Spill Level Cuts

##### Duty Factor

The beam structure is delivered in *bunches* of protons separated by 18.9ns. These bunches are better known as *RF buckets*, as they are synchronized with the 18.9ns cycle of the Fermilab RF clock. Ideally, each of these RF buckets deliver a steady number of protons per bucket.

In practice however, this is not the case, and not all the RF buckets delivered are occupied within a given spill. The fraction of buckets occupied is known as the accelerator Duty Factor,  $DF$ , and can be measured using a reference beam counter as

$$DF = \frac{\langle I \rangle^2}{\langle I^2 \rangle} \quad \text{with} \quad I = \sum_{N_{trig}} N_{X2T} \quad (5.1)$$

where  $N_{X2T}$  is the number of hits in the X2T



Bin#	$x_2$ Range
0	(0.08, 0.14]
1	(0.14, 0.16]
2	(0.16, 0.18]
3	(0.18, 0.21]
4	(0.21, 0.25]
5	(0.25, 0.31]
6	(0.31, 0.53]

Table 5.1:  $x_2$  bin ranges

target	yield
None	104
Empty	84
LH2	3138
LD2	3472
C	1721
Fe	1370
W	1553

Table 5.2: Raw dimuon yields for Roadset 57

### 5.2.2 Dimuon Level Cuts

### 5.2.3 Track Level Cuts

### 5.2.4 Other Cuts

## 5.3 Dimuon Yields

### 5.3.1 Binning of Data

The  $x_2$  bins for this EMC ratio measurement were chosen such that each bin in  $x_2$  has similar levels of statistics.

Concurrent with this analysis, studies of  $\bar{d}(x_2)/\bar{u}(x_2)$  and parton energy loss are conducted. Due to the nearly identical source of signal across these studies (good Drell-Yan target dimuons), a consistent selection of kinematic binning maintains a certain continuity among analyses. The  $x_2$  binning chosen can be found in Table 5.1

### 5.3.2 Raw Yields

The total number of target Drell-Yan events recorded for each target can be found in Table 5.2. The number of events broken down into

5.4 Rate Dependence and Combinatorial Background Correction

5.5 Empty/None Target Background Subtraction

5.6 Dimuon Yield Ratios

5.7  $ld_2$  Contamination Correction

5.8 Isoscalar Corrections for  $^{183}W$  and  $^{56}Fe$

## Chapter 6

# Results

## Chapter 7

# Discussion

## Chapter 8

# Conclusions

We conclude that Bryan Dannowitz likes coffee.

# Appendix A

## PMT Upgrades

### A.1 ARGUS PMT Performance 'Sag'

### A.2 Prototype Testing

### A.3 Manufacturing and Installation

## Appendix B

# MySQL Production Structure

### B.1 MySQL Servers

### B.2 Atomic Schema Design

### B.3 Merged Schemas

# References

- [1] D. M. Alde, H. W. Baer, T. A. Carey, G. T. Garvey, A. Klein, C. Lee, M. J. Leitch, J. W. Lillberg, P. L. McGaughey, C. S. Mishra, J. M. Moss, J. C. Peng, C. N. Brown, W. E. Cooper, Y. B. Hsiung, M. R. Adams, R. Guo, D. M. Kaplan, R. L. McCarthy, G. Danner, M. J. Wang, M. L. Barlett, and G. W. Hoffmann. Nuclear dependence of dimuon production at 800 gev. *Phys. Rev. Lett.*, 64(21):2479–2482, May 1990.
- [2] J.J. Aubert et al. The ratio of the nucleon structure functions  $F2_n$  for iron and deuterium. *Phys.Lett.*, B123:275, 1983.
- [3] S. D. Drell and Tung-Mow Yan. Massive Lepton Pair Production in Hadron-Hadron Collisions at High-Energies. *Phys. Rev. Lett.*, 25:316–320, 1970. [Erratum-ibid.25:902,1970].
- [4] Chun-Gui Duan, Na Liu, and Zhan-Yuan Yan. The extraction of nuclear sea quark distribution and energy loss effect in drell-yan experiment. *EUR.PHYS.J.C*, 50:585, 2007.
- [5] I. Estermann, R. Frisch, and O. Stern. Magnetic Moment of the Proton. *Nature*, 132:169–170, jul 1933.
- [6] R.W. Fast et al. 14.4 m large aperture analysis magnet with aluminum coils. Technical Report FERMILAB-TM-1034, Fermilab, 2015.
- [7] Donald F. Geesaman, K. Saito, and Anthony William Thomas. The nuclear EMC effect. *Ann.Rev.Nucl.Part.Sci.*, 45:337–390, 1995.
- [8] E. A. Hawker et al. Measurement of the light antiquark flavor asymmetry in the nucleon sea. *Phys. Rev. Lett.*, 80:3715–3718, Apr 1998.
- [9] HCZ Photonics. *XP2072: High energy resolution , 10-stage, 39mm (1.5”) tube*.
- [10] G. Moreno, C. N. Brown, W. E. Cooper, D. Finley, Y. B. Hsiung, A. M. Jonckheere, H. Jostlein, D. M. Kaplan, L. M. Lederman, Y. Hemmi, K. Imai, K. Miyake, T. Nakamura, N. Sasao, N. Tamura, T. Yoshida, A. Maki, Y. Sakai, R. Gray, K. B. Luk, J. P. Rutherford, P. B. Straub, R. W. Williams, K. K. Young, M. R. Adams, H. Glass, and D. Jaffe. Dimuon production in proton-copper collisions at  $\sqrt{s} = 38.8$  gev. *Phys. Rev. D*, 43(9):2815–2835, May 1991.
- [11] J. Pumplin et al. New generation of parton distributions with uncertainties from global QCD analysis. *JHEP*, 07:012, 2002.
- [12] J. Seely et al. New measurements of the EMC effect in very light nuclei. *Phys. Rev. Lett.*, 103:202301, 2009.
- [13] R. S. Towell et al. Improved measurement of the anti-d/anti-u asymmetry in the nucleon sea. *Phys. Rev.*, D64:052002, 2001.
- [14] N.S. Lockyer W.M. Bokhari, J.G. Heinrich and F.M. Newcomer. The ASDQ ASIC. *Nuclear Science Symposium, 1998 Conference Record*, 1:445–446, 1998.
- [15] T. Zimmerman and J. Hoff. The design of a charge integrating, modified floating point ADC chip. *IEEE J. Solid State Circuits*, 39:895–905, 2004.